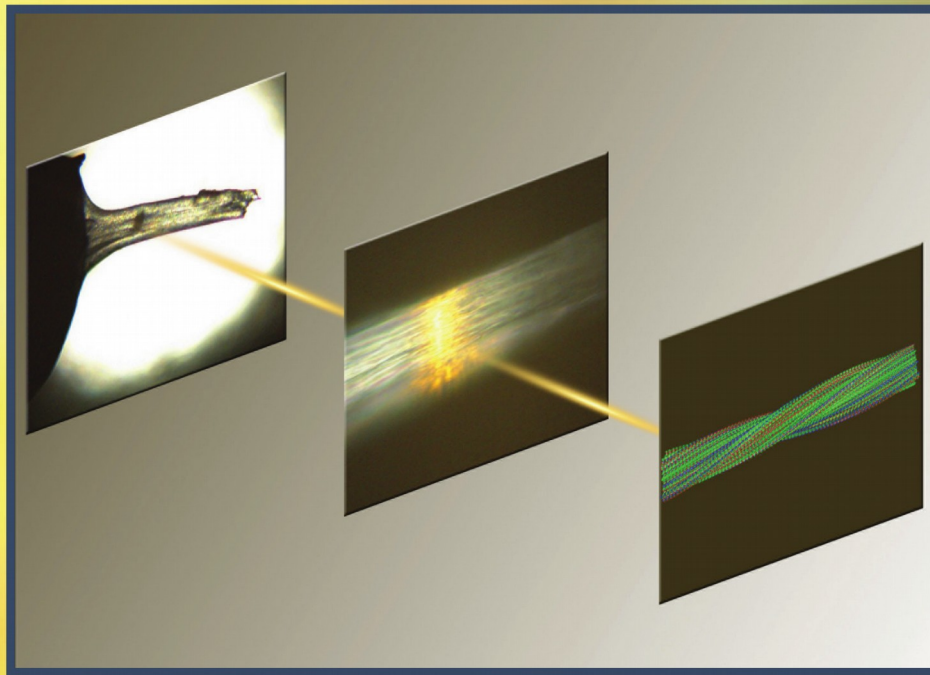


Volume 199, Issue 2, August 2017

ISSN 1047-8477

# Journal of Structural Biology

---



Available online at [www.sciencedirect.com](http://www.sciencedirect.com)

**ScienceDirect**



Contents lists available at ScienceDirect

# Journal of Structural Biology

journal homepage: [www.elsevier.com/locate/yjsbi](http://www.elsevier.com/locate/yjsbi)



## Volume 199, Issue 2, August 2017

### CONTENTS

Ting Wang, Yang Wang, Leihan Tang, Yong Duan, Haiguang Liu. $7 \times 7$ RMSD matrix: A new method for quantitative comparison of the transmembrane domain structures in the G-protein coupled receptors .....	87
Diana B. Peckys, Christof Stoerger, Lorenz Latta, Ulrich Wissenbach, Veit Flockerzi, Niels de Jonge. The stoichiometry of the TMEM16A ion channel determined in intact plasma membranes of COS-7 cells using liquid-phase electron microscopy .....	102
Jie He, Chyongere Hsieh, Yongping Wu, Thomas Schmelzer, Pan Wang, Ying Lin, Michael Marko, Haixin Sui. Cryo-FIB specimen preparation for use in a cartridge-type cryo-TEM .....	114
Christopher J. Peddie, Marie-Charlotte Domart, Xenia Snetkov, Peter O'Toole, Banafshe Larijani, Michael Way, Susan Cox, Lucy M. Collinson. Correlative super-resolution fluorescence and electron microscopy using conventional fluorescent proteins <i>in vacuo</i> .....	120
Meagan Cauble, Phillip Yang, Ulrich Baumann, Jan M. Gebauer, Bradford G. Orr, Le T. Duong, Mark M. Banaszak Holl. Microstructure dependent binding of pigment epithelium derived factor (PEDF) to type I collagen fibrils .....	132
Nikolaos N. Louros, Paraskevi L. Tsiolaki, Fotis A. Baltoumas, Georgios D. Chryssikos, Vassilis Gionis, Stavros J. Hamodrakas, Vassiliki A. Iconomidou. Tracking the amyloidogenic core of IAPP amyloid fibrils: Insights from micro-Raman spectroscopy	140
Mikhail Burke, Ahmad Golaraei, Ayelet Atkins, Margarete Akens, Virginijus Barzda, Cari Whyne. Collagen fibril organization within rat vertebral bone modified with metastatic involvement .....	153

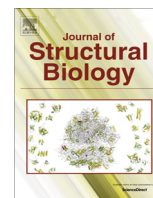
**Front Cover:** A glimpse into the three-dimensional structure of human islet amyloid polypeptide (IAPP) amyloid fibrils. *Louros et al.* expose IAPP amyloid fibers to a micro-Raman laser line in distinct orientations and assess the structural moieties that contribute as vital parts of the amyloid fibril core.

For a full and complete Guide for Authors, please go to: <http://www.elsevier.com/locate/yjsbi>

Abstracted/indexed in Biological Abstracts, Chemical Abstracts, Current Contents/Life Sciences, EMBASE, EMBiology, Excerpta Medica, MEDLINE® Research Alert, SCISEARCH, Science Citation Index. Also covered in the citation database Scopus®. Full text available on ScienceDirect®



1047-8477(201708)199:2;1-U



## Tracking the amyloidogenic core of IAPP amyloid fibrils: Insights from micro-Raman spectroscopy



Nikolaos N. Louros<sup>a,1</sup>, Paraskevi L. Tsiolaki<sup>a</sup>, Fotis A. Baltoumas<sup>a</sup>, Georgios D. Chryssikos<sup>b</sup>, Vassilis Gionis<sup>b</sup>, Stavros J. Hamodrakas<sup>a</sup>, Vassiliki A. Iconomidou<sup>a,\*</sup>

<sup>a</sup>Section of Cell Biology and Biophysics, Department of Biology, School of Sciences, National and Kapodistrian University of Athens, Panepistimiopolis, Athens 157 01, Greece

<sup>b</sup>Theoretical and Physical Chemistry Institute, National Hellenic Research Foundation, Athens 116 35, Greece

### ARTICLE INFO

#### Article history:

Received 22 February 2017

Received in revised form 19 May 2017

Accepted 3 June 2017

Available online 14 June 2017

#### Keywords:

Amylin

Amyloidosis

Aggregation-prone peptides

Disulfide bonds

Type II diabetes

Raman Spectroscopy

### ABSTRACT

Human islet amyloid polypeptide (hIAPP) is the major protein component of extracellular amyloid deposits, located in the islets of Langerhans, a hallmark of type II diabetes. The underlying mechanisms of IAPP aggregation have not yet been clearly defined, although the highly amyloidogenic sequence of the protein has been extensively studied. Several segments have been highlighted as aggregation-prone regions (APRs), with much attention focused on the central 8–17 and 20–29 stretches. In this work, we employ micro-Raman spectroscopy to identify specific regions that are contributing to or are excluded from the amyloidogenic core of IAPP amyloid fibrils. Our results demonstrate that both the N-terminal region containing a conserved disulfide bond between Cys residues at positions 2 and 7, and the C-terminal region containing the only Tyr residue are excluded from the amyloid core. Finally, by performing detailed aggregation assays and molecular dynamics simulations on a number of IAPP variants, we demonstrate that point mutations within the central APRs contribute to the reduction of the overall amyloidogenic potential of the protein but do not completely abolish the formation of IAPP amyloid fibrils.

© 2017 Elsevier Inc. All rights reserved.

### 1. Introduction

Islet amyloid polypeptide (IAPP), or amylin, is a 37-residue pancreatic hormone produced and secreted along with insulin as a response to high levels of glucose within the bloodstream. IAPP is a highly amyloidogenic peptide, primarily associated with the development of type II diabetes (Clark et al., 1987; Cooper et al., 1987). IAPP accumulation within the islets of Langerhans eventually causes  $\beta$ -cell dysfunction and death, consequently leading to reduced insulin secretion (Westermarck and Wilander, 1978; Westermarck et al., 1987a). The toxic effect of hIAPP is a subject of controversy, in which amyloid-mediated membrane damage is

*Abbreviations:* hIAPP, human IAPP; rIAPP, rat IAPP; APRs, aggregation-prone regions; STEM, scanning-transmission electron microscopy; ssNMR, solid-state Nuclear Magnetic Resonance; RMSF, root mean square fluctuation; ASA, accessible surface area; TERS, Tip-Enhanced Raman Spectroscopy.

\* Corresponding author.

*E-mail addresses:* [nlouros@biol.uoa.gr](mailto:nlouros@biol.uoa.gr) (N.N. Louros), [etsiolaki@biol.uoa.gr](mailto:etsiolaki@biol.uoa.gr) (P.L. Tsiolaki), [fbaltoumas@biol.uoa.gr](mailto:fbaltoumas@biol.uoa.gr) (F.A. Baltoumas), [gdchryss@eie.gr](mailto:gdchryss@eie.gr) (G.D. Chryssikos), [vgionis@eie.gr](mailto:vgionis@eie.gr) (V. Gionis), [shamodr@biol.uoa.gr](mailto:shamodr@biol.uoa.gr) (S.J. Hamodrakas), [veconom@biol.uoa.gr](mailto:veconom@biol.uoa.gr) (V.A. Iconomidou).

<sup>1</sup> Present address: VIB Switch Laboratory, Department of Cellular and Molecular Medicine, VIB-KU Leuven, B-3000 Leuven, Belgium.

<http://dx.doi.org/10.1016/j.jsb.2017.06.002>

1047-8477/© 2017 Elsevier Inc. All rights reserved.

considered to play a key role. A two-fold mechanism of aggregation has been proposed, suggesting that initial membrane disruption is caused by early oligomeric IAPP species that can also template amyloid fiber formation on the membrane surface at a later stage, a process leading to subsequent fragmentation (Brender et al., 2012; Patel et al., 2014; Sciacca et al., 2016). The N-terminal 1–19 region of the peptide is primarily responsible for membrane binding by controlling the orientation and penetration depth of the molecule in respect to the membrane surface (Nanga et al., 2009). On the other hand, almost the entire sequence of human IAPP has been denoted as an aggregation-prone region (APR), suggesting that the aggregation effect of the protein may not be as straightforward as expected (Azriel and Gazit, 2001; Fox et al., 2010; Lutz, 2010; Marek et al., 2007). Several lines of evidence have focused at the aggregation potential of the 20–29 central segment. Comparison studies reveal significant differences in the structure, function and toxicity kinetics between the corresponding regions of human and rat IAPP sequences (hIAPP<sub>20–29</sub> and rIAPP<sub>20–29</sub>) (Brender et al., 2007, 2013). This is mostly attributed to the fact that the non-amyloidogenic rIAPP<sub>20–29</sub> sequence comprises three individual Pro residues within this range, imparting its overall aggregation tendency (Christoffersen et al., 2015; Madine et al., 2008; Moriarty and Raleigh, 1999; Westermarck

et al., 1990). An amylin replacement has been developed based on this strategy and is currently administered along with insulin in patients with type I and II diabetes (Ratner et al., 2004).

Although accumulating evidence suggests that IAPP is intrinsically disordered or partially  $\alpha$ -helical in its active and functional form (Nanga et al., 2011; Williamson and Miranker, 2007), the structural properties of IAPP monomers incorporated in amyloid fibrils are yet poorly understood. Detailed NMR structural studies on human and rat peptides have highlighted that the 1–19 region of the molecule is primarily  $\alpha$ -helical, suggesting that helical intermediates promote the overall toxicity of IAPP by facilitating membrane disruption (Brender et al., 2010; Nanga et al., 2009). Up to date, a number of theoretical or experimental studies have proposed possible models regarding the fibrillar core of human IAPP amyloid fibrils. A parallel superpleated structure, composed of three individual  $\beta$ -strands was initially proposed (Kajava et al., 2005), followed by ssNMR and STEM observations suggesting that the 8–17 and 28–37 segments of the protein compose the main fibril core (Luca et al., 2007). This model was also supported subsequently by two-dimensional infrared spectroscopy (IR) studies (Shim et al., 2009). Finally, a third model has also been proposed, relying on the atomic structures of segments 21–27 and 28–33 which were suggested to form tight steric zippers with closely interdigitated side chains (Wiltzius et al., 2008).

In this work, we applied micro-Raman spectroscopy on aligned IAPP amyloid fibrils to extract information about the structural elements that are part of the amyloidogenic core, in addition to the conformational states and orientation of individual moieties, such as the N-terminally located intermolecular disulfide bridge, the  $\beta$ -sheet content and the C-terminal Tyr side chains of the IAPP monomers. Furthermore, we performed detailed aggregation assays on several variants focused around the major 8–17 and 20–29 APRs of the IAPP sequence. These results are complemented with Molecular Dynamics (MD) simulations and discussed in comparison with the existing reported models regarding IAPP amyloid fibrils.

## 2. Materials and methods

### 2.1. Aggregation propensity prediction

The aggregation propensity of human IAPP was investigated through sequence analysis, with the aid of the consensus aggregation propensity predictor, AMYLPRED2 (Tsolis et al., 2013). This consensus tool produces a multivariate prediction of sequence amyloidogenicity by incorporating individual algorithms, focused on identifying variable physicochemical properties associated with aggregation propensity, such as sequence hydrophobicity, packing density, “chameleon” segments and amyloidogenic sequence stretches (Conchillo-Sole et al., 2007; Fernandez-Escamilla et al., 2004; Kim et al., 2009; Tian et al., 2009).

### 2.2. Peptide synthesis

The synthesis of human wild type (WT) IAPP and its mutated derivatives (Fig. 1) was performed by GeneCust (Luxembourg). All peptides were prepared with amidated C-terminal ends and free N-terminals (purity >95%). IAPP<sub>1–12</sub> (free N- and C-terminal) was prepared by solid phase methodology and Fmoc/Bu<sup>t</sup> chemistry, using 2-chlorotrityl chloride resin as a solid support (Barlos et al., 1989). Analytical HPLC was utilized in order to determine peptide purity (>97%).

### 2.3. Preparation of peptide samples and oriented fibers

Solution samples of IAPP and its derivatives were prepared at a concentration of 0.5 mg/ml, in distilled water. The IAPP<sub>1–12</sub> peptide

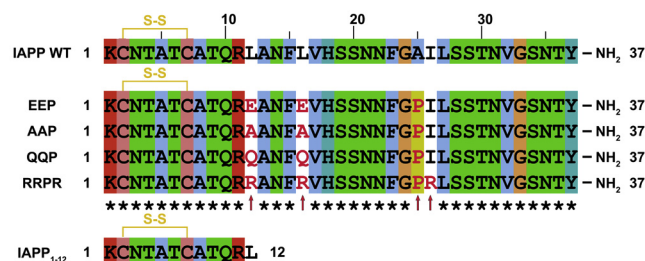


**Fig. 1.** Sequence of human IAPP and its mutated derivatives. Four different variants were designed by replacing residues L12 and L16 to charged, polar or other hydrophobic residues (EEP, RRPR, QQP and AAP peptides). All peptides have a single substitution of A25P, whereas the RRPR peptide also incorporates an additional I26R mutation. All variants were C-terminal amidated and contained an intramolecular disulfide bond (shown in yellow brackets). A peptide analogue of the N-terminal segment of IAPP was also designed (IAPP<sub>1–12</sub>).

segment was dissolved at peptide concentrations up to 10 mg/ml. Oriented fibers containing more or less aligned amyloid fibrils were prepared after 1–2 weeks of incubation at ambient temperature, by applying a droplet (5  $\mu$ l) of each peptide solution between aligned glass rods with silicone-covered ends, spaced approximately 2 mm apart. The droplets were slowly air-dried at ambient conditions to produce oriented fibers suitable for X-ray diffraction and micro-Raman spectroscopic analysis. IAPP<sub>1–12</sub> solutions were incubated for long periods of up to six months, however were incapable of forming well-oriented fibers. As a result, suspensions of this peptide were cast on a front-coated Au mirror and left to dry in ambient conditions to form films suitable for micro-Raman measurements.

### 2.4. Transmission electron microscopy

Suspensions of each peptide were placed on carbon-coated copper grids and allowed to sit for 60 s. Subsequently, the grids were flash-washed with distilled water and stained with a drop of 2% (w/v) aqueous uranyl acetate for 45 s. Excess stain was removed by blotting with a filter paper. A Morgagni<sup>TM</sup> 268 transmission electron microscope, operated at 80 kV, was used for examination of prepared grids. Digital micrographs were acquired with an 11 Mpixel, side-mounted Morada CCD camera (Soft Imaging System, Muenster, Germany).

### 2.5. X-ray diffraction

X-ray diffraction patterns were collected from oriented fibers, using a SuperNova-Agilent Technologies X-ray generator, operated at 50 kV and 0.8 mA, equipped with a 135-mm ATLAS CCD detector and a 4-circle kappa goniometer (CuK $\alpha$  high intensity X-ray micro-focus source,  $\lambda = 1.5418$  Å). Specimen-to-film distance was specified at 52 mm, whereas exposure time was set to 400 s. Initial viewing was performed using the program CrysAlisPro (Oxford Diffraction, 2009). The X-ray diffraction patterns were measured and displayed with the aid of iMosFLM (Leslie and Powell, 2007).

### 2.6. Congo red staining assays

Drops of all peptide solutions were applied to glass slides and air-dried at ambient conditions, producing hydrated films. A Congo red solution (1% w/v) was prepared in distilled water and used to stain the hydrated films, following previous protocols (Louros et al., 2014, 2015a; Romhanyi, 1971). Excess stain was removed by rinsing in water (Romhanyi, 1971). Stained samples were observed under bright field illumination and between crossed polars, utilizing a Leica MZ7.5 polarizing stereomicroscope

equipped with a JVC GC-X3E camera. Congo Red spectrophotometric assays were also carried out for the WT and its corresponding variants. Absorption spectra ranging from 400 to 700 nm (every 50 nm) were recorded every 5 min at room temperature for a period of one (1) hour, following a detailed protocol (Nilsson, 2004). Congo Red spectra (50  $\mu$ M) were obtained as a reference, subsequently mixed with the peptide sample solution (10  $\mu$ M) and measured. Spectral acquisitions were performed by a BIO-RAD SmartSpec™ 3000 Spectrophotometer (170–2501), with polystyrene disposable cuvettes (1 cm optical length).

### 2.7. Micro-Raman spectroscopy

Oriented fibers of IAPP and its mutant variants were measured by micro-Raman spectroscopy, in two distinct orientations (Fig. S1). Specifically, measurements were obtained for a parallel orientation between the fiber and laser line polarization axes. Measurements of a perpendicular orientation were also obtained, after switching the fiber axis by 90°, relative to the polarization axis. Micro-Raman spectra were recorded on a dispersive confocal Raman microscope (Renishaw InVia Reflex, 1200 L/mm). Data were collected through a 50 $\times$  lens using a 785 nm diode laser line for excitation. Several spectra were obtained over the 450–1750  $\text{cm}^{-1}$  Stokes range per sample and averaged. The total acquisition time was of the order of 1 h per sample to improve signal-to-noise ratio. Second derivative analysis was utilized in order to determine accurately the position of the sharp vibrational bands (Iconomidou et al., 2000).

### 2.8. Molecular dynamics simulations

Initial coordinates for IAPP in protofibril configuration were obtained from a previously described model structure, derived from ssNMR measurements and STEM observations (Luca et al., 2007). The model features ten copies of IAPP, organized in two pentamers interacting with one another in an antiparallel fashion, resulting in a final structure adopting a C2 rotational symmetry around the fibril axis. Protomers adopt a  $\beta$ -strand – loop –  $\beta$ -strand (U-bend) fold and form pentamers by interacting through intermolecular hydrogen bonds. The first  $\beta$ -strand is formed by residues in the 8–16 region, while the second strand is larger, involving the 27–37 region. Overall, approximately 55% of the structure adopts a  $\beta$ -sheet conformation.

System setup and modeling were performed using Visual Molecular Dynamics (VMD) (Humphrey et al., 1996) and the CHARMM36 topology (Huang and MacKerell, 2013). Mutations were introduced through the *Mutate residue* function in VMD, followed by a short energy minimization to remove steric clashes. Disulfide bonds were formed between Cys-2 and Cys-7 and the protomer C-termini were amidated. Each protofibril model was embedded in a solvent box with a margin of at least 15 Å from the boundaries to any protofibril particle and a NaCl ion concentration of 0.15 M. The final size of each system was approximately ~64,000–65,000 particles.

Molecular Dynamics (MD) simulations were performed in the isothermal – isobaric (NPT) ensemble using periodic boundary conditions. Temperature was maintained at 310 K using Langevin dynamics with a damping coefficient of 1  $\text{ps}^{-1}$ , while pressure was controlled at 1 atm using the Nosé-Hoover Langevin piston barostat, with an oscillation period of 100 fs and a decay rate of 50 fs (Feller et al., 1995). All covalently bonded hydrogen atoms were constrained with the RATTLE and SETTLE algorithms for proteins and water, respectively (Andersen, 1983; Miyamoto and Kollman, 1992; Ryckaert et al., 1977), enabling the use of a 2 fs time step. Short range non-bonded interactions were calculated using switching functions between 10 and 12 Å, while long range

electrostatic interactions were screened using the Particle Mesh Ewald (PME) method.

All simulations were performed using NAMD v. 2.11 (Phillips et al., 2005) and the CHARMM36 all-atom force field (Huang and MacKerell, 2013). The systems were subjected to 5000 steps of energy minimization and were gradually equilibrated over 1 ns, applying restraints of gradually decreasing strength on the protein atoms. Finally, each system was simulated without restraints for 100 ns. Two independent production simulations were performed per setup for validation, initialized with randomized velocity. The total simulation time of the study accumulates to approximately 1  $\mu$ s. Simulation results were analyzed using VMD and DSSP (Kabsch and Sander, 1983).

## 3. Results

### 3.1. Tracking the amyloidogenic potential of IAPP

Sequence analysis of IAPP revealed two major central regions with high aggregation potential. The prominent APR is composed primarily of residues of the 8–17 region, which has been previously highlighted as a major amyloidogenic segment along the IAPP sequence (Jaikaran et al., 2001; Laghaei et al., 2011; Louros et al., 2015b; Mao et al., 2016; Mazor et al., 2002; Scrocchi et al., 2003). The second segment, comprising residues 20–29, is one of the first documented APRs of the IAPP sequence (Christoffersen et al., 2015; Madine et al., 2008; Moriarty and Raleigh, 1999; Westermark et al., 1990). Minimal aggregation potency is observed for both the N-terminal and C-terminal regions of the protein, although previous aggregation assays have linked the C-terminal part of the protein with possible amyloidogenicity (Jaikaran et al., 2001).

Strategically placed mutations within the central APRs were predicted, with the aid of AMYLPRED2, to reduce the overall aggregation potency of the protein to a significant extent (Figs. 1 and 2). Previous theoretical and structural studies have indicated that the 8–17 region constitutes a hydrophobic interface which may be crucial for IAPP self-assembly (Fox et al., 2010; Guo et al., 2015; Laghaei et al., 2011; Louros et al., 2015a). Towards this end, IAPP variants were designed and synthesized, introducing a double replacement of the L12 and L16 residues of this hydrophobic interface. Variants with conserved substitutions, such as L12A-L16A (AAP) or, to a lesser extent, L12Q-L16Q (QQP), were predicted to have a mildly reduced amyloidogenic potential (Fig. 2). On the other hand, substitution of prominent hydrophobic residues by charged residues, such as L12E-L16E (EEP) or L12R-L16R-I26R (RRPR), was predicted to impart greater reduction in the overall amyloidogenicity of the protein (Fig. 2). The aggregation tendency of the 20–29 region was reduced by introducing an A25P mutation in all cases (Figs. 1 and 2), following the example of previous studies (Green et al., 2003; Wang et al., 2015).

### 3.2. Aggregation assays of hIAPP variants

The reduction in amyloidogenicity caused by mutations introduced in the central APRs was initially monitored with electron microscopy and X-ray diffraction. Electron microscopy studies revealed that all IAPP variants were actually capable of forming mature amyloid filaments through self-assembly (Fig. 3), in spite of the calculated reduction of their amyloidogenic potential. Impressively, the presence of charged residues did not interrupt the fibrillation process, since both the EEP and RRPR peptides form amyloid fibrils with morphologies comparable to those of the wild type hormone (Fig. 3B and E). More specifically, both peptides form 10–12 nm wide amyloid fibrils with a strong tendency for lateral

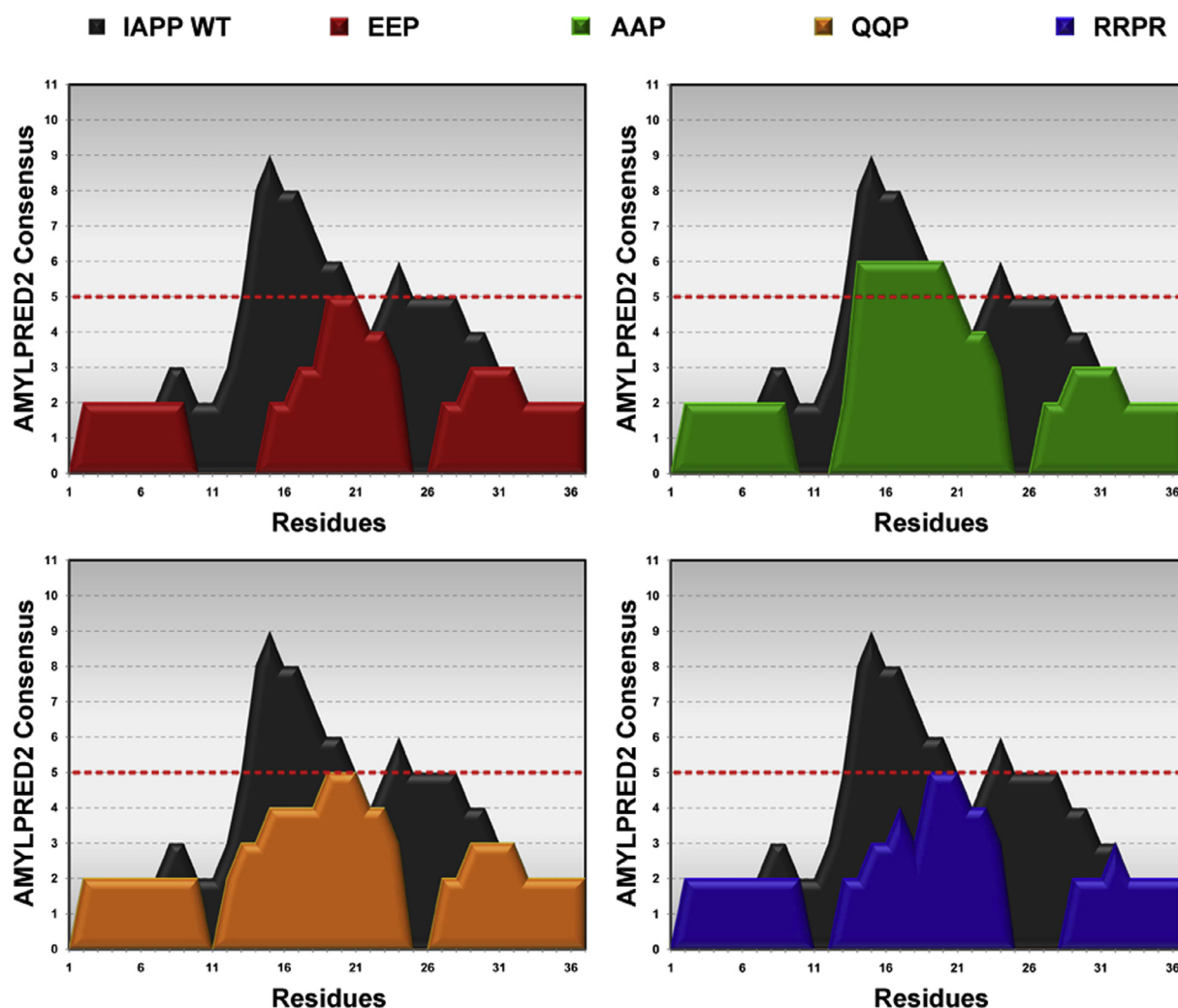


**Fig. 2.** Amyloidogenic potential of the four IAPP variants, compared to WT IAPP. The WT protein exhibits two major APRs, specifically regions 8–17 and 20–29. An A25P mutation, present in all mutants, significantly decreases the predicted amyloidogenic potential of the second APR. Substitution of the high scoring L12 and L16 residues also results in a reduction of the amyloidogenic potential of the 8–17 region, with the insertion of charged residues having the most significant effect, such as in the case of EEP (red) and RRPR (blue). Residue positions are indicated in the horizontal axis, whereas the AMYLPRED2 consensus prediction is shown on the vertical axis. Positive prediction by 5 out of 11 algorithms is set as a default cut-off value (shown in red lines).

attachments leading to the formation of thick fibrillar networks. This effect is intensified during the self-aggregation process of the QQP peptide which leads towards the formation of thick gels (Fig. 3D), suggesting that conserved substitutions might instead lead to an increase in the aggregation potential of the protein. It is noteworthy that, despite its increased amyloidogenicity, the AAP peptide forms shorter fibrous structures compared to the WT hormone (Fig. 3C). The above indicate that the structural and physicochemical alterations applied with the above mutations are not sufficient to inhibit the aggregation tendency of the central APRs found within the IAPP sequence, although a change in morphology occurs in some cases.

Although some studies suggest otherwise (Green et al., 2003), our results are in line with theoretical evidence indicating that all three proline substitutions found in pramlintide, the pharmaceutical replacement of IAPP (A25P-S28P-S29P), are required in order to successfully slow down IAPP aggregation (Chiu et al., 2013). Together, the aggregation assays indicate that the hydrophobic interface of the 8–17 central region may be an important but not binding factor during IAPP fibrillation, since even the presence of charged or bulky residues did not seem to impart the process to a full scale.

The “cross- $\beta$ ” architecture of the fibrils formed by the self-aggregating variants was verified through X-ray diffraction. The specific amino acid substitutions do not seem to alter the overall structure of the IAPP amyloid fibril core, since all variants produce typical “cross- $\beta$ ” patterns, similar to the diffraction pattern produced from WT IAPP amyloid fibrils (Fig. 3F–J). Specifically, a meridian reflection corresponding to the 4.7Å periodicity between hydrogen-bonded  $\beta$ -strands is observed in all cases. Surprisingly, a 10.1 Å equatorial reflection is also observed, indicating that substitution of the Leu residues does not result to significant changes in the packing distance between the corresponding successive  $\beta$ -sheet. However, the presence of charged Glu, and to a less extent Arg residues, disarranges the formed EEP and RRPR fibers, thus producing non-oriented diffraction patterns with reflections appearing as rings (Fig. 3G and J).

### 3.3. Congo red spectroscopy reveals differences in the aggregation kinetics between IAPP variants

Congo red has been shown to selectively bind on amyloid fibrils, producing a diagnostic yellow/green birefringence when viewed under crossed polars of a polarizing microscope (Divry and

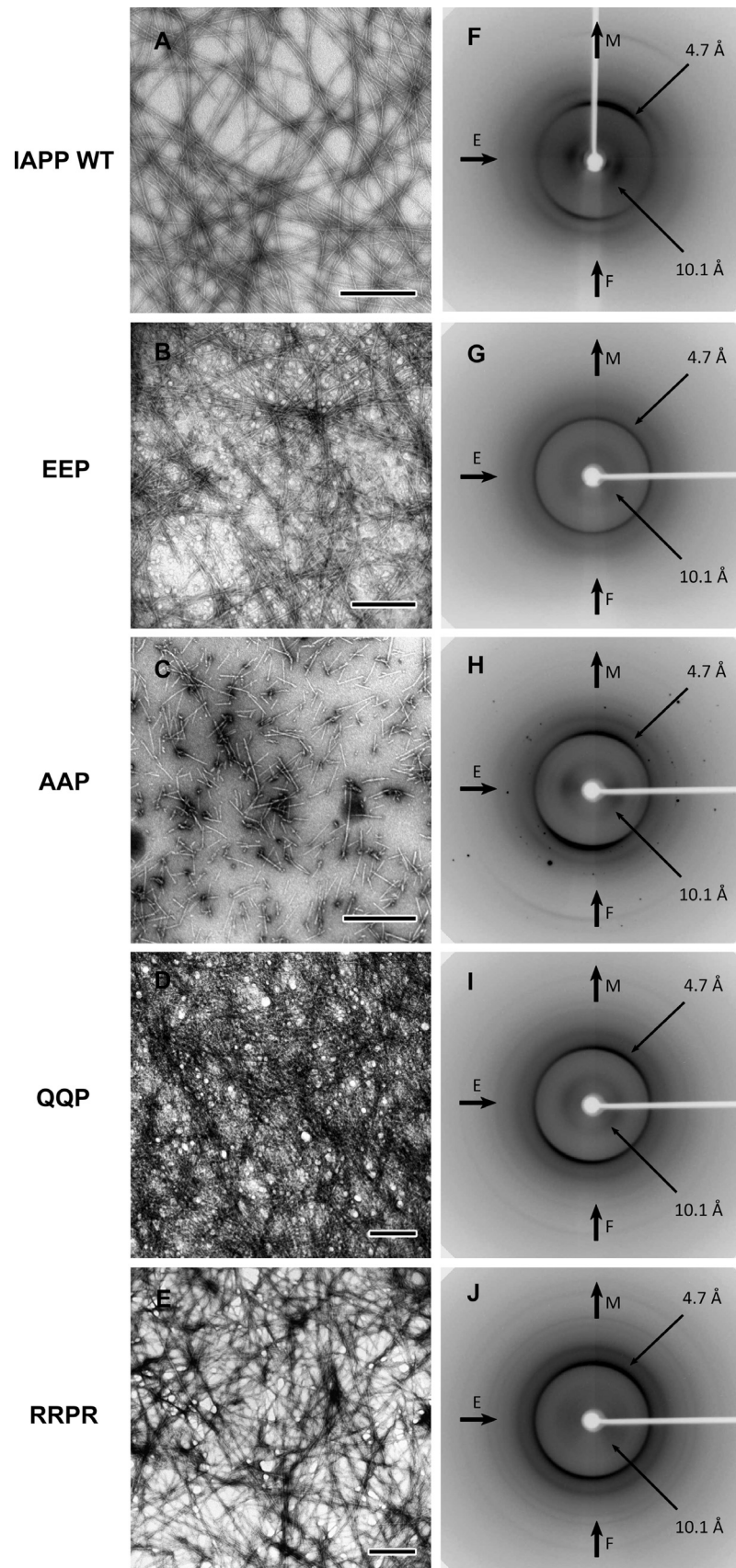


**Fig. 3.** Electron micrographs (A-E) and X-ray diffraction patterns (F-J) of amyloid fibrils formed by WT IAPP and the corresponding variants. Closely similar amyloid-like morphologies of 10–12 nm wide amyloid fibrils with no interconnections and indeterminate lengths are observed for the WT and variants, with the AAP peptide forming fibrils with shorter lengths (Scale bars 500 nm). Both the WT protein and the variants produce comparable cross- $\beta$  patterns. Charged residues (G, J) affect the alignment of the formed fibers, resulting in a less oriented pattern with reflections appearing as rings (M: meridian; E: equator; F: fibril axis).

Florkin, 1927). Deposits containing the amyloid-like fibrils of all corresponding variants were capable of binding the Congo red dye, as viewed under bright field illumination (Fig. 4A). Moreover, when switched to crossed polars, the stained deposits clearly display characteristic apple-green birefringence, thus certifying the amyloidogenic properties of the fibrils. Congo red binding was also confirmed by spectroscopic kinetic analysis. The Congo red dye exhibits maximum absorbance at 500 nm, which was confirmed by control studies of a 50  $\mu$ M solution sample (Fig. 4B, black curves). However, when bound to the surface of amyloid fibrils, the dye exhibits an evident shift in its maximal absorbance to 540 nm. All IAPP variants were capable of shifting the absorbance maximum of the dye, after incubation for 60 min (Fig. 4B, dark blue line), suggesting that the formation of amyloid-like fibers has occurred, whereas no shift was witnessed immediately after dissolving the peptides (Fig. 4B, dark red line).

Similar kinetics were monitored for the QQP peptide with minimal differences, whereas the AAP shifting was completed after only the first 10 min of incubation, verifying that the L12A-L16A mutations increased the aggregation rate of the protein. On the other hand, although the presence of charged residues did not completely hinder the aggregation propensity of the protein, it did lead to a significant decrease in the rate of fibrillation. More specifically, shifting for the RRPR peptide occurs after 20 min, such as in the case of the QQP peptide, however no increase was observed at 540 nm after the first 10 min of incubation. As expected, the introduction of negatively charged residues, as in the case of the EEP peptide, resulted in a 3-fold decrease of the fibrillation rate compared to the WT hormone, since a shift was detected only after 50 min of incubation. The above indicate that the presence of charged residues within the APRs of IAPP produce less favorable aggregation interactions, in line with studies proposing that such residues may act as gatekeepers against amyloid aggregation (Beerten et al., 2012; Sant'Anna et al., 2014). However, even significant alterations of the physicochemical properties of the 8–17 APR are not able to suppress the aggregation propensity of the molecule, suggesting that the hydrophobic interface of the 8–17 region is probably not the only major driving force behind IAPP fibrillation.

#### 3.4. Micro-Raman spectroscopy provides evidence of the aggregation-prone core of IAPP amyloid fibrils

Raman spectroscopy is a powerful non-invasive technique for the structural characterization of protein aggregates, including amyloids, where traditional methods, such as X-ray crystallography or NMR are inapplicable (Ortiz et al., 2007; Rodriguez-Perez et al., 2013; Sereda et al., 2015). This technique has been applied in the past to determine the orientation of individual structural units within the sample (Rousseau et al., 2004). Here, micro-Raman spectroscopy was applied on the oriented amyloid fibers of the IAPP variants (Fig. S2). This analysis enabled the study of the conformational properties of certain structural units of IAPP and yielded information about the orientation and contribution of these structures in the amyloid core of IAPP fibrils (Fig. 5).

##### 3.4.1. Amide I region (1550–1750 $\text{cm}^{-1}$ )

As expected, the WT protein, as well as all the variants, exhibits a strong amide I band at 1671–1672  $\text{cm}^{-1}$ , attributed to the well-ordered  $\beta$ -sheet secondary structure of the formed amyloid fibrils. Additional component bands located at  $\sim$ 1585 and  $\sim$ 1605  $\text{cm}^{-1}$  are assigned to the ring modes of Phe and Tyr residues. Detailed evidence was also extracted regarding the uniformity and orientation level of the amyloid fibers formed by each peptide. The amide I Raman band depends primarily on the C=O stretching mode (Chen et al., 1994; Mirkin and Krimm, 1991). The C=O groups are ori-

ented more or less in a parallel fashion to the main fibril axis, since they take part in the formation of hydrogen bonds between successive  $\beta$ -strands composing the cross- $\beta$  amyloid fibril core. Significant differences were observed between the intensities of the amide I bands for parallel and perpendicularly oriented WT, AAP and QQP fibers, indicating the formation of uniform and well-oriented fibers. This indication is in good agreement with the well-oriented diffraction patterns of the same samples (Fig. 3). In contrast, the EEP and RRPR peptides present no differences in the intensity of the amide I band between parallel and perpendicular orientations. This probably suggests a more or less random orientation of the constituent amyloid fibrils. It is noteworthy that identical intensities between the parallel and perpendicular orientations could also occur in the highly unlikely event of the total number of constituent fibrils aligned at exactly 45° relative to the polarization axis of the laser.

##### 3.4.2. Tyrosine residues (800–900 $\text{cm}^{-1}$ )

Tyrosine residues are responsible for a doublet appearing in this range, due to Fermi resonance between the ring-breathing vibration and the overtone of an out-of-plane ring bending vibration of the *para*-substituted phenolic side chain (Siamwiza et al., 1975). Furthermore, the relative peak intensity ratio ( $R = I_{850}/I_{830}$ ) strongly depends on the ionization state of the phenoxy group and is sensitive to its participation in H-bonding, therefore it is commonly used to inspect the burial or exposure of Tyr residues (Carey, 1982). All variants include a single Tyr right next to their C-terminal end and present a characteristic doublet, at 851–856  $\text{cm}^{-1}$  and 830–838  $\text{cm}^{-1}$ . For WT, EEP, AAP and QQP peptides, a  $R \sim 1.25$  value indicates that the C-terminal Tyr acts as both a donor and an acceptor of moderate hydrogen bonds. The corresponding ratio on RRPR is just slightly lower than 1, indicating that in this case Tyr has a slightly stronger role as a hydrogen donor.  $R$  values ranging from 1.25 to 1.40 indicate that the Tyr residues are exposed and not buried, thus unlikely to contribute to the buried hydrophobic amyloid core (Carey, 1982). The WT peptide has a relatively unusual character, containing three distinct bands at 830, 841 and 856  $\text{cm}^{-1}$ .

It has been reported previously that Tyr heterogeneity within aggregates could lead to a splitting of one of the vibrational modes, resulting in 3 peaks instead of the conventional doublet (Pandit et al., 2008). This is also supported by the increased ratio of the 841  $\text{cm}^{-1}$  peak relative to the doublet in the perpendicular orientation, implying several conformations for the C-terminal Tyr residue between different protomers composing WT amyloid fibrils. Notably, this splitting event for the 841  $\text{cm}^{-1}$  peak occurs at the expense of the 830  $\text{cm}^{-1}$  band, a feature that is significantly stronger in the perpendicular orientation. No evidence for splitting was displayed by the variants. This could suggest that the corresponding substitutions may have a stabilizing effect in the conformation of the Tyr residue compared to the WT. On the other hand, this lack of splitting could be due to increased disorder (in comparison to the WT). Increased disorder may not allow for resolving the two components, causing instead, a shift of the derivative minimum within the 830–840  $\text{cm}^{-1}$  range. Finally, no significant differences of the doublet intensity were observed between the two orientations. This observation supports the hypothesis that the C-terminally placed Tyr residue is not part of the stable vital cross- $\beta$  core of IAPP amyloid fibrils.

##### 3.4.3. Disulfide bonds (450–560 $\text{cm}^{-1}$ )

Vibrational modes in this range are directly affected by different conformations of disulfide bridges (Nakanishi et al., 1974; Van Wart et al., 1973). The presence of characteristic peaks at 489–492, 505–510 and 520–527  $\text{cm}^{-1}$  verifies that the fibrillation process maintains but influences the disulfide bridge of the WT and

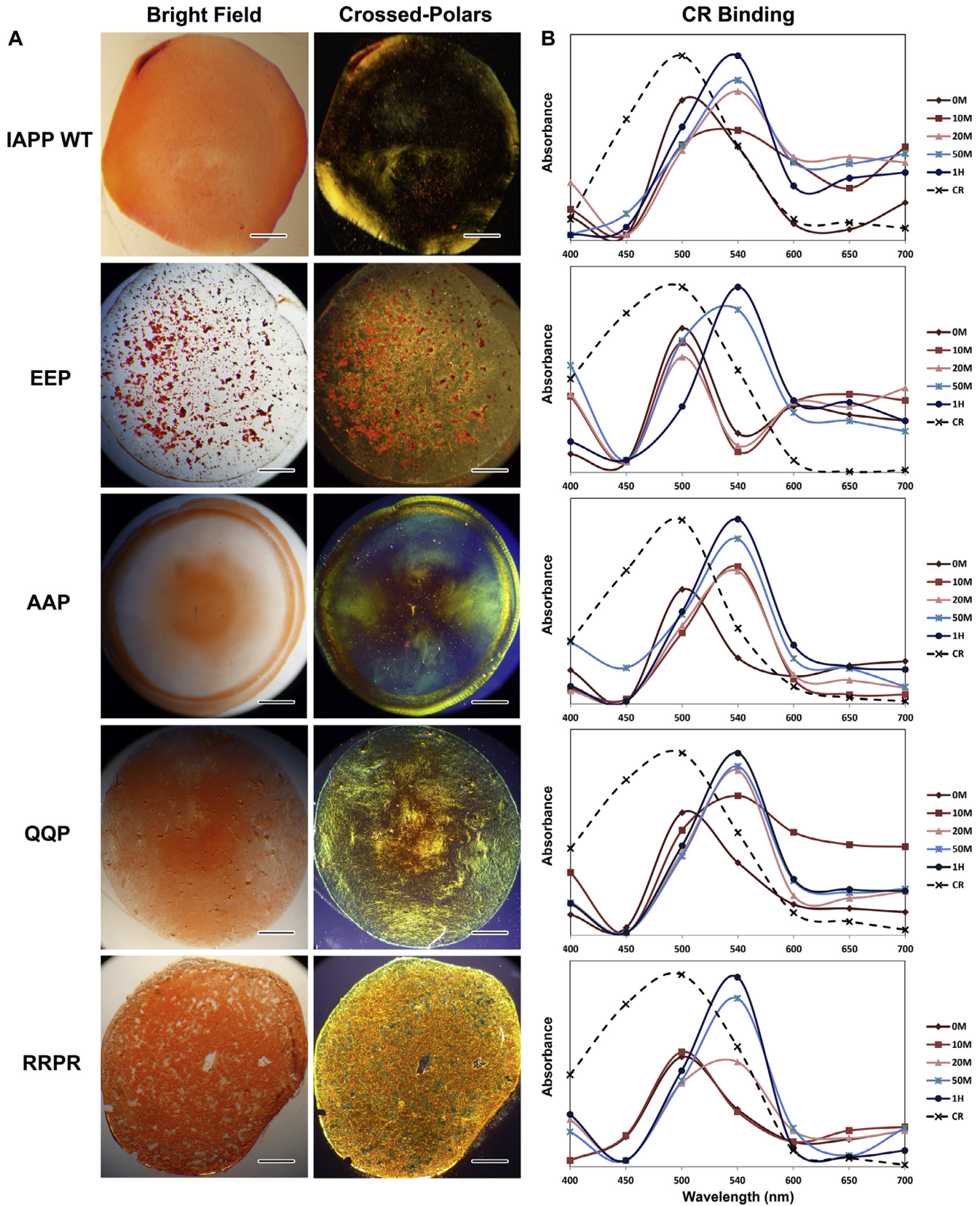


**Fig. 4.** Congo red binding assays of IAPP variants. (A) The amyloidogenic properties of the WT protein and its variants were confirmed by their ability to bind the CR, as seen under bright field illumination and the apple-green birefringence when switching to crossed-polars (Scale bars 400  $\mu$ m). (B) CR binding studies revealed slower rates of fibrillation for the EEP and RRPR peptides and an accelerated rate of fibril formation for the AAP peptide, compared to the WT protein. The CR reference curves, showing a maximum absorbance at 500 nm are shown in black dotted lines in each graph.

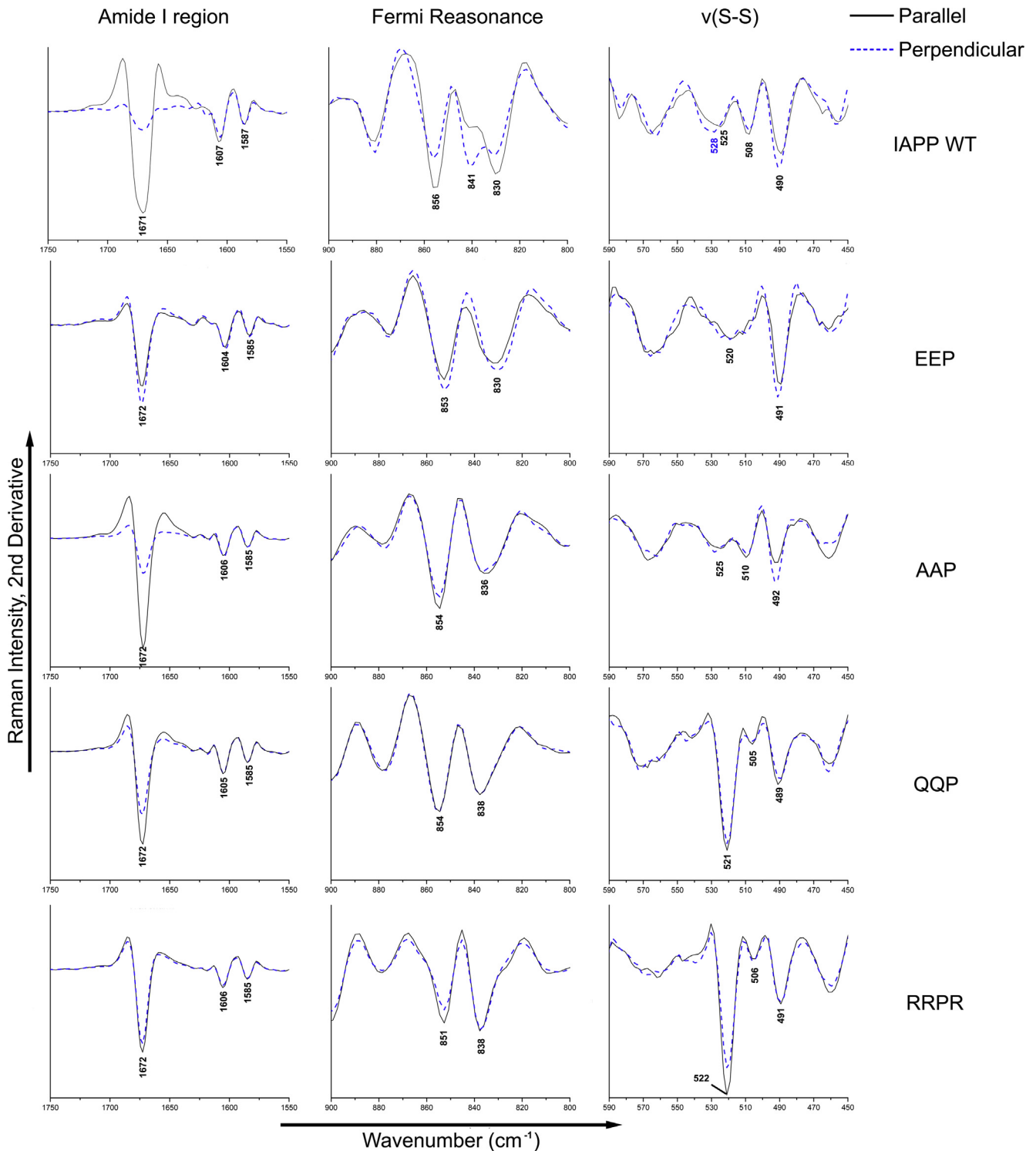


**Fig. 5.** Second derivative micro-Raman spectra obtained from parallel (black line) and perpendicular (blue line) arrangements between IAPP variant amyloid fibers and the laser polarization axis. Analysis of the amide I region reveals that all peptides participate in the formation of uniform and stable  $\beta$ -sheet structures. Noticeable intensity differences among orientations illustrate the formation of well-oriented fibers containing WT, AAP and QQP amyloid fibrils. The characteristic Fermi doublet (800–900 cm<sup>-1</sup>) reveals that the C-terminal Tyr residue most probably serves as a donor and acceptor to the formation of moderate hydrogen bonds.  $I_{850}/I_{830}$  ratios suggest that the Tyr side chains are predominantly exposed rather than buried within the fibril core. The splitting event observed in the spectra of the WT peptide indicates high conformational heterogeneity between the Tyr side chains. The absence of differences in the intensities between parallel and perpendicular orientations of the well-oriented WT, AAP and QQP variants is clearly evident. Several bands are observed in the 450–560 cm<sup>-1</sup> region of the spectra, suggesting multiple conformations for the disulfide bridges. The component at 490 cm<sup>-1</sup> arises as a result of low CS-SC angles, signifying that the disulfide bridges are under mechanical strain. For visualization purposes, the 800–900 cm<sup>-1</sup> and 450–540 cm<sup>-1</sup> regions are shown expanded by factors of 3.5x and 10x, respectively, relative to the amide I region.

its variants. The two latter peaks are assigned to S-S stretching vibrations (v(S-S)) of disulfide bridges found in a *gauche-gauche-*

*gauche* (ggg) and *gauche-gauche-trans* (ggt or tgg) conformation (Sugeta, 1975; Sugeta et al., 1972, 1973), indicating multiple con-

formations for the CS-SC group for protomers incorporated within the formed fibrils. The additional component located at  $\sim 490\text{ cm}^{-1}$  has been suggested to arise from a CS-SC moiety with a low dihedral angle (Van Wart and Scheraga, 1976). Low disulfide bridge dihedral angles occur as a result of strain to the bond, suggesting that the formation of IAPP amyloid fibrils causes mechanical stress on the N-terminal disulfide bond of the WT protomers. The relative intensities of the three peaks in WT and EEP indicate that almost half of the monomers of the amyloid fibers contain strained disulfide bridges. The strain level is lower for the AAP peptide, where all three conformations seem to have a more or less equal contribution. Finally, the strain of the disulfide bond seems to be limited in the case of the QQP and RRPR peptides, where more than half of the bridges appear to adopt a ggt/tgg conformation.

The hypothesis concerning the association of fibrillation with the stress of the disulfide bond was further supported by the analysis of micro-Raman spectra derived from films formed by the IAPP<sub>1-12</sub> peptide segment (Fig. S3). Specifically, no band was observed close to  $\sim 490\text{ cm}^{-1}$ , suggesting that no strain was present in the absence of fibrillation (Table S1). However, multiple conformations of disulfide bridges were detected, as the presence of two bands disclosed, again with a preference for the ggt/tgg conformation ( $\sim 3:5$  ratio) (Fig. S3). The aforementioned results indicate that the intramolecular disulfide bridges of the N-terminal segment of IAPP and the corresponding variants do not adopt a single conformation and are under stress during fibrillation, therefore most probably do not contribute as a pivotal part of the stable amyloid fibril core. The conformational instability of the disulfide bond is also evident through the spectral shift of the  $525\text{ cm}^{-1}$  band to  $528\text{ cm}^{-1}$ , observed between the two orientations for the hIAPP fiber (Fig. 5). Analysis of the data obtained between different orientations further support this hypothesis. Specifically, minimal or no changes were observed by comparing the intensities of the peaks between a parallel and a perpendicular orientation. This is a strong indication that, at least for the well oriented WT, AAP and QQP fibers, the N-terminal part of the monomers, containing the intramolecular disulfide bond, is not incorporated within the amyloid fibril core.

### 3.5. Comparison with existing models of IAPP fibril structures

Explicit solvent MD simulations were performed for the WT and variant protofibrils, adopting a previously suggested configuration (Luca et al., 2007). Analogous substitutions were performed for L12, L16 and A25 for the AAP, QQP and EEP systems, while an additional substitution of I26R was introduced in the RRPR system. Notably, the above residues are buried in the hydrophobic core with the exception of A25.

Simulations of the WT protofibril were reasonably stable, with minimal changes in the overall fold. The parallel, in-register  $\beta$ -strands and the U-shaped topology of the peptides were retained, with the monomers adopting a twist of  $\sim 4\text{--}6^\circ$  between adjacent  $\beta$ -strands, in agreement with experimentally observed axial fibril twists (Fig. 6A). Tight packing of side chains was observed in the experimentally verified 8–17 and 20–29 APRs composing the first  $\beta$ -strand, the turn region and the beginning of the facing  $\beta$ -strand, proposing favorable interactions for these segments (Fig. 6A and B). Structural analysis of the modelled structure provides information on the importance of the Ser residue located in position 20 of the IAPP sequence. A S20G mutation is commonly associated with early onset type II diabetes in Asian populations (Sakagashira et al., 2000). Previous theoretical studies have suggested that the S20G mutation can possibly promote IAPP aggregation by destabilizing the early  $\alpha$ -helical content of IAPP monomers, driving it towards an extended  $\beta$ -strand conformation (Duan et al., 2012; Wang et al., 2012). Furthermore, studies have also high-

lighted that the critical position of a S20G mutation is capable of inducing local flexibility and reducing the overall entropy cost for the assembly process (Xu et al., 2009), providing a possible explanation for the faster aggregation kinetics induced by the S20G mutation. The overall  $\beta$ -sheet content remains stable at approximately 55%. Orientation of the two pentamers was maintained, suggesting further favorable interactions between the 23–29 segments of two entities. An average Root Mean Square Deviation (RMSD) value of  $5.3\text{ \AA}$  was measured for the final 10 ns of the simulations; this value is in good agreement with evidence from previous, shorter MD simulations of human IAPP protofibril pentamers (Liang et al., 2013a). Root Mean Square Fluctuation (RMSF) measurements (per-residue analysis) validated the order and stability of the 8–16 and 24–30 segments, which showed minimal fluctuations (Fig. S4) compared to the overall structure. In contrast, both the N- and C-termini displayed high RMSF and Accessible Surface Area (ASA) values accounting for extensive mobility of these regions (Figs. S4 and S5). Coupled with the slight disordering observed in the C-terminal 34–37 segment, these results further verify the notion that the N- and C-ends of the monomers are not vitally contributing in the stable IAPP amyloid fibril core.

Similar behaviors were observed during the AAP and QQP variant simulations, with both systems retaining their initial protofibril configurations. The overall packing and secondary structure elements were preserved, as revealed by  $\beta$ -sheet content (%) and ASA ( $\text{\AA}^2$ ) analysis (Table 1). The conserved L12A and L16A substitutions did not disrupt the hydrophobic core of the steric zipper, thus allowing the system to incorporate the double mutation and remain stable. Furthermore, the A25P substitution located at the end of the turn connecting the facing strands allowed the incorporation of Pro residues stacked along the fibril axis, and facilitated the U-bend overall fold. During the QQP simulation, the protomers adopted specific features that allow the incorporation of stacked Gln residues in the hydrophobic core. More specifically, buried Q12 side chains increased the packing density of the steric zipper. This process was facilitated by the formation of a tight hydrogen bond network between stacked Q12 side chains, in close proximity to the equally buried T30 side chains of the facing  $\beta$ -strand, resulting in the formation of more stable pentamers (Fig. 6C). Both systems exhibited similar fluctuations, compared to the WT, indicating that they also contain amyloidogenic cores. In contrast to the above, significant disruptions for the protofibrils were observed in the RRPR and EEP simulations. In both cases the 8–17  $\beta$ -strand of the protomers dissociated, with certain segments partially reverting to a helical structure, leading to an opening of the U-bend and destruction of the overall protofibril fold. These results highlight the inability of the system to accommodate buried charged side chains that disrupt the hydrophobic interior of the protofibril core. Taken together, these results would suggest that the proposed protofibril structure is not compatible with the fibril properties of EEP and RRPR. However, in both the EEP and the RRPR simulations, the  $\beta$ -sheets of the 24–30 segments and the packing of the pentamers remain intact, indicating that despite the applied substitutions, these particular regions retain their amyloid-like features. Furthermore, it is important to note that the initial model corresponds to a specific polymorph of hIAPP amyloid fibrils (Luca et al., 2007). Therefore, it is possible that IAPP self-assembly includes different stabilizing interactions between polymorphs with different properties, allowing variants such as the EEP and RRPR peptides to form amyloid fibrils with alternative morphologies. This notion is also supported by several studies showing that monomeric IAPP is capable of interconverting between various conformations during the initial stages of aggregation and is associated to a number of putative overlapping aggregation pathways (Chiu and de Pablo, 2015; Dupuis et al., 2011;

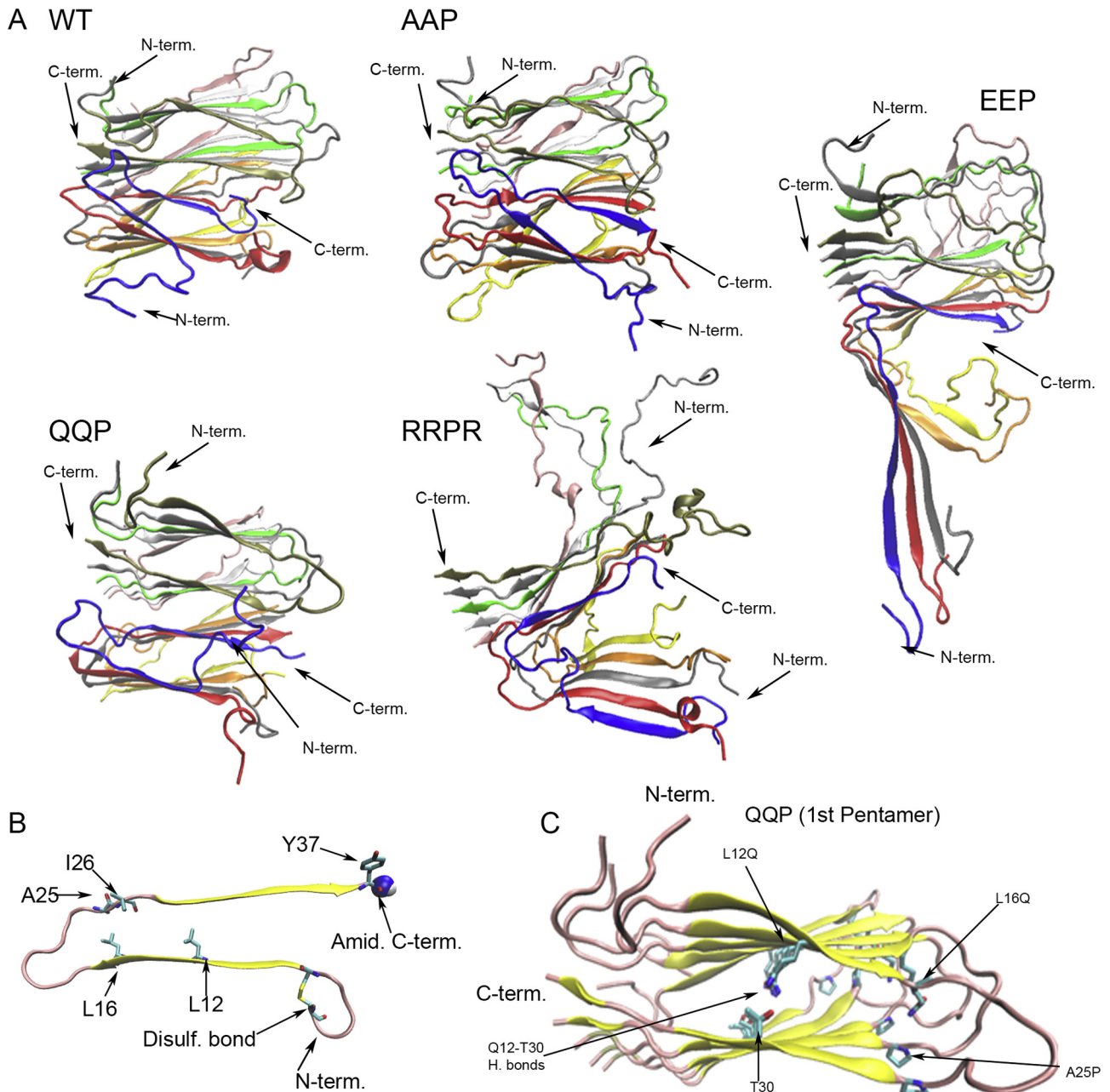


**Fig. 6.** Structural overview of the IAPP protofibril simulation systems. (A) Representations of the simulated WT and mutant protofibrils after 100 ns of MD simulations. All structures are shown in the same orientation using a cartoon representation, with each IAPP monomer colored differently. Solvent molecules are not rendered for clarity. N- and C-termini of the first protomer in each pentamer are labeled. (B) Features of IAPP, depicted upon the structure of an isolated monomer. The monomer is colored according to secondary structure elements, using yellow for  $\beta$ -strands and pink for unstructured regions. Positions of point mutations, the C2–C7 disulfide bond and the C-terminal Tyr are depicted as sticks and colored using cyan for carbon, blue for nitrogen and red for oxygen atoms. Hydrogen atoms were excluded for clarity. The amidated C-terminus is shown in sphere representation and colored blue for nitrogen and white for hydrogen atoms. (C) Close inspection of the first pentamer for the QQP simulation after 100 ns. Secondary structure elements and residue depictions are shown as in (B). Amino acid substitutions, as well as T30 are shown and labeled accordingly. The favorable packing of side chains and a potential hydrogen bond network between Q12 and T30 is indicated.

**Table 1**  
Summary of simulation systems with structural characteristics, averaged over the last 10 ns of the simulations.

System	Substitutions	Number of particles	RMSD (Å)	Backbone hydrogen bonds	% $\beta$ -sheet content	Normalized ASA (Å <sup>2</sup> ) <sup>a</sup>
WT	–	64545	5.30 ± 0.13	171 ± 4	56.54 ± 0.96	1736.70 ± 173.25
AAP	L12A-L16A-A25P	64224	5.65 ± 0.19	176 ± 3	55.14 ± 1.09	1743.03 ± 158.05
QQP	L12Q-L16Q-A25P	64328	4.95 ± 0.12	174 ± 4	56.15 ± 1.10	1663.16 ± 177.82
EEP	L12E-L16E-A25P	64322	18.60 ± 0.36	144 ± 4	39.63 ± 2.55	2184.23 ± 196.10
RRPR	L12R-L16R-A25P-I26R	64735	19.43 ± 0.37	137 ± 4	29.86 ± 2.86	2633.23 ± 237.76

<sup>a</sup> Per-protomer Accessible Surface Area (ASA), averaged over all protomers in the protofibril.

Liang et al., 2013b). Both experimental and computational studies have highlighted that the 8–16 segment of IAPP, primarily  $\alpha$ -helical in the initial fold, may participate in early dimerization events (Abedini and Raleigh, 2009; Laghaei et al., 2011), suggesting that the EEP and RRPR mutations could possibly influence the balance of the IAPP aggregation pathway, leading to the formation of fibrils with alternative morphological characteristics.

#### 4. Discussion

Evidence accumulated over the years has linked several segments of human IAPP with its aggregation propensity. Early studies highlighted that human IAPP, as a member of the calcitonin gene related peptide family, shares reasonable sequence homology to  $\alpha$ - and  $\beta$ -calcitonin gene related peptides (CGRPs), adrenomedullin and intermedin, especially at the N- and C-termini (Cooper et al., 1987; Westermark et al., 1987b). However, IAPP is the only documented member of the family capable of forming amyloid fibrils. IAPP differs from the members of the CGRP family primarily in the 20–29 region, suggesting that this region plays a vital role during its aggregation (Westermark et al., 1990). Supplementary experiments with rIAPP initially confirmed that IAPP amyloidogenicity is possibly controlled by this region, attributing the inability of the latter to aggregate to the presence of 3 Pro residues within this segment (Betsholtz et al., 1989). However, recent contradictory data reveal that the proline mutations do not completely inhibit IAPP aggregation, which still occurs but at slower rates (da Silva et al., 2016). The hydrophobic interface of the amphipathic 8–17 segment of IAPP is also considered as major driving force of IAPP fibrillogenesis, thus increasing further the complexity behind IAPP aggregation (Jaikaran et al., 2001; Laghaei et al., 2011; Louros et al., 2015b; Mao et al., 2016; Mazor et al., 2002; Scrocchi et al., 2003). Following the above, several studies focused at identifying specific mutations along the IAPP sequence which can eliminate its aggregation tendency (Abedini and Raleigh, 2006; Green et al., 2003; Koo et al., 2008), expanding the possible aggregation prone sites along its entire sequence (Fox et al., 2010). Even the end terminal regions of the protein, which were initially considered to be protective against IAPP fibrillation (Koo and Miranker, 2005; Tu et al., 2014) have been at some point associated to the formation of fiber-like structures (Cope et al., 2013; Jaikaran and Clark, 2001).

Sequence analysis utilizing AMYLPRED2 verified that the 8–17 and 20–29 segments of IAPP present the highest predicted amyloidogenic potential. Accordingly, mutations targeted to reduce the hydrophobic potential and amyloidogenic properties of the 8–17 and 20–29 segments were introduced. Impressively, significant alterations of the 8–17 segment were incapable of inhibiting IAPP aggregation, supporting the hypothesis that this is not the only segment controlling IAPP aggregation. However, the hydrophobic nature of this segment most probably participates in the formation of the amyloid fibril core, since the presence of charged residues leads to 3-fold slower rate of IAPP fibrillation, as shown by the CR kinetic experiments. On the other hand, the presence of a single Pro residue at position 25 also was not capable of reducing the amyloidogenic potential of the 20–29 segment, in line with supplementary evidence suggesting that the A25P substitution lowers the  $\beta$ -propensity of the protein, yet, retains some amyloidogenic characteristics (Chakraborty et al., 2013; Chiu et al., 2013). MD simulations highlighted that the cyclic structural features of its side chain, may allow the Pro residue occupying position 25 to promote the stability of the fibril core, by facilitating the turn region between the facing  $\beta$ -strands.

The main focus of this study was to identify which segments of human IAPP are indeed part of or excluded from the stable hydrophobic core of human IAPP amyloid fibrils. For this purpose,

micro-Raman spectroscopy was employed given its sensitivity to the single intramolecular disulfide bond (C2-C7) and the single Tyr residue (Y37) that occupy the N- and C-termini of the molecule, respectively. The micro-Raman spectra of the AAP and QQP fibers are very similar to those of the WT, suggesting that the specific mutations do not alter significantly the structural properties of the amyloid fibrils. On the other hand, the presence of charged residues affected the orientation and uniformity of the fibrils, indicating less favorable interactions than in the WT protein and suggesting that the 8–17 APR segment may be incorporated as part of the amyloid core.

Different conformations were observed for the disulfide bridges of all peptides, including WT. These data suggest that the N-terminal region of IAPP that contains the intermolecular disulfide bridge is not incorporated within the stable hydrophobic core. However, IAPP fibrillation was found to cause mechanical stress on the disulfide bridges of the peptide monomers, as revealed by the shifting of disulfide bands to lower energies, suggesting that this segment is directly affected by fibrillogenesis. Interestingly, the C2-C7 disulfide bridge is positioned next to the 8–17 APR along the IAPP sequence. Incorporation of this segment within the amyloid core could possibly explain the strain applied on the monomer disulfide bridges. These findings are in agreement with recent studies suggesting that the disulfide bond is important in containing IAPP aggregation, rather than being part of the fibril core (Iltchev et al., 2016).

Analysis of the Fermi resonance doublet revealed that the C-terminal Tyr is surface exposed, in agreement with recent TERS results (vandenAkker et al., 2015). Moreover, the micro-Raman spectra of the WT fibers were found to exhibit an unusual splitting event, attributed to the presence of different Tyr conformations. This variability suggests that the C-terminal residue of the protein is highly unlikely to be part of the stable amyloid core.

#### 5. Conclusions

Micro-Raman spectroscopy provided valuable information regarding the structural features of human IAPP amyloid fibrils. The spectroscopic data validate the hypothesis that the hydrophobic core of human IAPP amyloid fibrils is most probably composed by the central APRs of the sequence, whereas the N- and C-terminal ends of the protein are more or less excluded. However, the alteration of the hydrophobic properties of the 8–17 APR segment, as well as a single Pro substitution of the 20–29 APR at position 25 did not prove sufficient to impart IAPP fibrillogenesis, suggesting that these factors are not sufficient for controlling IAPP aggregation. Future experiments should be focused on identifying the underlying forces that lead these central segments towards the formation of the IAPP amyloid fibril core.

#### Conflict of interest

The authors declare no conflicts of interest.

#### Funding

<sup>1</sup>This research has been co-financed by the European Union (European Regional Development Fund – ERDF) and Greek national funds through the Operational Program ‘Competitiveness and Entrepreneurship’ of the National Strategic Reference Framework (NSRF) (Project code 11SYN-1-1230, General Secretariat for Research and Technology of the Greek Ministry of Education and Religious Affairs, Culture and Sports). <sup>2</sup>Research at TPCI/NHRF was supported through funds of its Applied Spectroscopy Laboratory. <sup>3</sup>This work was supported by computational time granted

from the Greek Research & Technology Network (GRNET) in the National HPC facility – ARIS under project ID “PRO02041-S.C.S.M.P.”.

## Acknowledgments

We would like to thank Dr. Sorin Luca and Dr. Robert Tycko for kindly providing the coordinates of the initial IAPP fibril model. We thank Assist. Prof. Vassiliki Magafa and Dr. Aikaterini Zompra from the University of Patras for the synthesis of the IAPP<sub>1–12</sub> peptide. We thank Costas Tsiantos for expert technical assistance in Micro-Raman Spectroscopy. We thank the Institute of Biology, Medicinal Chemistry and Biotechnology at National Hellenic Research Foundation for access to the X-ray diffraction facility. We acknowledge the help of Dr. Evangelia Chrysinia with the X-ray diffraction experiments. The help of Dr. George Baltatzis and Prof. Efstratios Patsouris and the use of the Morgagni Microscope at the 1st Department of Pathology, Medical School, National and Kapodistrian University of Athens are also gratefully acknowledged. Finally, we would like to thank the handling editor and the anonymous reviewers of this manuscript for their useful and constructive criticism.

## Appendix A. Supplementary data

Supplementary data associated with this article can be found, in the online version, at <http://dx.doi.org/10.1016/j.jsb.2017.06.002>.

## References

- Abedini, A., Raleigh, D.P., 2006. Destabilization of human IAPP amyloid fibrils by proline mutations outside of the putative amyloidogenic domain: is there a critical amyloidogenic domain in human IAPP? *J. Mol. Biol.* 355, 274–281.
- Abedini, A., Raleigh, D.P., 2009. A critical assessment of the role of helical intermediates in amyloid formation by natively unfolded proteins and polypeptides. *Protein Eng. Des. Sel.* 22, 453–459.
- Andersen, H.C., 1983. Rattle: a “velocity” version of the shake algorithm for molecular dynamics calculations. *J. Comput. Phys.* 52, 24–34.
- Azriel, R., Gazit, E., 2001. Analysis of the minimal amyloid-forming fragment of the islet amyloid polypeptide. An experimental support for the key role of the phenylalanine residue in amyloid formation. *J. Biol. Chem.* 276, 34156–34161.
- Barlos, K., Gatos, D., Kallitsis, J., Papaphotiu, G., Sotiriou, P., Wenqing, Y., Schäfer, W., 1989. Darstellung geschützter peptid-fragmente unter einatz substituierter triphenylmethyl-harze. *Tetrahedron Lett.* 30, 3943–3946.
- Beerten, J., Jonckheere, W., Rudyak, S., Xu, J., Wilkinson, H., De Smet, F., Schymkowitz, J., Rousseau, F., 2012. Aggregation gatekeepers modulate protein homeostasis of aggregating sequences and affect bacterial fitness. *Protein Eng. Des. Sel.* 25, 357–366.
- Betsholtz, C., Christmansson, L., Engstrom, U., Rorsman, F., Svensson, V., Johnson, K. H., Westermark, P., 1989. Sequence divergence in a specific region of islet amyloid polypeptide (IAPP) explains differences in islet amyloid formation between species. *FEBS Lett.* 251, 261–264.
- Brender, J.R., Durr, U.H., Heyl, D., Budarapu, M.B., Ramamoorthy, A., 2007. Membrane fragmentation by an amyloidogenic fragment of human Islet Amyloid Polypeptide detected by solid-state NMR spectroscopy of membrane nanotubes. *Biochim. Biophys. Acta* 1768, 2026–2029.
- Brender, J.R., Hartman, K., Nanga, R.P., Popovych, N., de la Salud Bea, R., Vivekanandan, S., Marsh, E.N., Ramamoorthy, A., 2010. Role of zinc in human islet amyloid polypeptide aggregation. *J. Am. Chem. Soc.* 132, 8973–8983.
- Brender, J.R., Salamekh, S., Ramamoorthy, A., 2012. Membrane disruption and early events in the aggregation of the diabetes related peptide IAPP from a molecular perspective. *Acc. Chem. Res.* 45, 454–462.
- Brender, J.R., Heyl, D.L., Samisetti, S., Kotler, S.A., Osborne, J.M., Pesaru, R.R., Ramamoorthy, A., 2013. Membrane disordering is not sufficient for membrane permeabilization by islet amyloid polypeptide: studies of IAPP(20–29) fragments. *Phys. Chem. Chem. Phys.* 15, 8908–8915.
- Carey, P.R., 1982. *Biochemical Applications of Raman and Resonance Raman Spectroscopies*. Academic Press.
- Chakraborty, S., Mukherjee, B., Basu, S., 2013. Pinpointing proline substitution to be responsible for the loss of amyloidogenesis in IAPP. *Chem. Biol. Drug Des.* 82, 446–452.
- Chen, X.G., Schweitzer-Stenner, R., Krimm, S., Mirkin, N.G., Asher, S.A., 1994. N-methylacetamide and its hydrogen-bonded water molecules are vibrationally coupled. *J. Am. Chem. Soc.* 116, 11141–11142.
- Chiu, C.C., de Pablo, J.J., 2015. Fibrillar dimer formation of islet amyloid polypeptides. *AIP Adv.* 5, 092501.
- Chiu, C.C., Singh, S., de Pablo, J.J., 2013. Effect of proline mutations on the monomer conformations of amylin. *Biophys. J.* 105, 1227–1235.
- Christoffersen, H.F., Andreasen, M., Zhang, S., Nielsen, E.H., Christiansen, G., Dong, M., Skrydstrup, T., Otzen, D.E., 2015. Scaffolded multimers of hIAPP(20–29) peptide fragments fibrillate faster and lead to different fibrils compared to the free hIAPP(20–29) peptide fragment. *Biochim. Biophys. Acta* 1854, 1890–1897.
- Clark, A., Cooper, G.J., Lewis, C.E., Morris, J.F., Willis, A.C., Reid, K.B., Turner, R.C., 1987. Islet amyloid formed from diabetes-associated peptide may be pathogenic in type-2 diabetes. *Lancet* 2, 231–234.
- Conchillo-Sole, O., de Groot, N.S., Aviles, F.X., Vendrell, J., Daura, X., Ventura, S., 2007. AGGRESAN: a server for the prediction and evaluation of “hot spots” of aggregation in polypeptides. *BMC Bioinf.* 8, 65.
- Cooper, G.J., Willis, A.C., Clark, A., Turner, R.C., Sim, R.B., Reid, K.B., 1987. Purification and characterization of a peptide from amyloid-rich pancreases of type 2 diabetic patients. *Proc. Natl. Acad. Sci. U.S.A.* 84, 8628–8632.
- Cope, S.M., Shinde, S., Best, R.B., Ghirlanda, G., Vaiana, S.M., 2013. Cyclic N-terminal loop of amylin forms non amyloid fibers. *Biophys. J.* 105, 1661–1669.
- da Silva, D.C., Fontes, G.N., Erthal, L.C., Lima, L.M., 2016. Amyloidogenesis of the amylin analogue pramlintide. *Biophys. Chem.* 219, 1–8.
- Divry, D., Florkin, M., 1927. Sur les propriétés optiques de l’amyloïde. *C. R. Soc. Biol.* 97, 1808–1810.
- Duan, M., Fan, J., Huo, S., 2012. Conformations of islet amyloid polypeptide monomers in a membrane environment: implications for fibril formation. *PLoS One* 7, e47150.
- Dupuis, N.F., Wu, C., Shea, J.-E., Bowers, M.T., 2011. The amyloid formation mechanism in human IAPP: dimers have  $\beta$ -strand monomer–monomer interfaces. *J. Am. Chem. Soc.* 133, 7240–7243.
- Feller, S.E., Zhang, Y., Pastor, R.W., Brooks, B.R., 1995. Constant pressure molecular dynamics simulation: the Langevin piston method. *J. Chem. Phys.* 103, 4613–4621.
- Fernandez-Escamilla, A.M., Rousseau, F., Schymkowitz, J., Serrano, L., 2004. Prediction of sequence-dependent and mutational effects on the aggregation of peptides and proteins. *Nat. Biotechnol.* 22, 1302–1306.
- Fox, A., Snollaerts, T., Errecart Casanova, C., Calciano, A., Nogaj, L.A., Moffet, D.A., 2010. Selection for nonamyloidogenic mutants of islet amyloid polypeptide (IAPP) identifies an extended region for amyloidogenicity. *Biochemistry* 49, 7783–7789.
- Green, J., Goldsbury, C., Mini, T., Sunderji, S., Frey, P., Kistler, J., Cooper, G., Aebi, U., 2003. Full-length rat amylin forms fibrils following substitution of single residues from human amylin. *J. Mol. Biol.* 326, 1147–1156.
- Guo, C., Cote, S., Mousseau, N., Wei, G., 2015. Distinct helix propensities and membrane interactions of human and rat IAPP(1–19) monomers in anionic lipid bilayers. *J. Phys. Chem. B* 119, 3366–3376.
- Huang, J., MacKerell Jr., A.D., 2013. CHARMM36 all-atom additive protein force field: validation based on comparison to NMR data. *J. Comput. Chem.* 34, 2135–2145.
- Humphrey, W., Dalke, A., Schulten, K., 1996. VMD: visual molecular dynamics. *J. Mol. Graph.* 14 (33–38), 27–38.
- Iconomidou, V.A., Chryssikos, D.G., Gionis, V., Pavlidis, M.A., Paipetis, A., Hamodrakas, S.J., 2000. Secondary structure of chorion proteins of the teleostean fish *Dentex dentex* by ATR FT-IR and FT-Raman spectroscopy. *J. Struct. Biol.* 132, 112–122.
- Ilitchev, A.I., Giammona, M.J., Do, T.D., Wong, A.G., Buratto, S.K., Shea, J.E., Raleigh, D. P., Bowers, M.T., 2016. Human islet amyloid polypeptide N-terminus fragment self-assembly: effect of conserved disulfide bond on aggregation propensity. *J. Am. Soc. Mass Spectrom.* 27, 1010–1018.
- Jaikaran, E.T., Clark, A., 2001. Islet amyloid and type 2 diabetes: from molecular misfolding to islet pathophysiology. *Biochim. Biophys. Acta* 1537, 179–203.
- Jaikaran, E.T., Higham, C.E., Serpell, L.C., Zurdo, J., Gross, M., Clark, A., Fraser, P.E., 2001. Identification of a novel human islet amyloid polypeptide beta-sheet domain and factors influencing fibrillogenesis. *J. Mol. Biol.* 308, 515–525.
- Kabsch, W., Sander, C., 1983. Dictionary of protein secondary structure: pattern recognition of hydrogen-bonded and geometrical features. *Biopolymers* 22, 2577–2637.
- Kajava, A.V., Aebi, U., Steven, A.C., 2005. The parallel superpleated beta-structure as a model for amyloid fibrils of human amylin. *J. Mol. Biol.* 348, 247–252.
- Kim, C., Choi, J., Lee, S.J., Welsh, W.J., Yoon, S., 2009. NetCSSP: web application for predicting chameleon sequences and amyloid fibril formation. *Nucleic Acids Res.* 37, W469–473.
- Koo, B.W., Miranker, A.D., 2005. Contribution of the intrinsic disulfide to the assembly mechanism of islet amyloid. *Protein Sci.* 14, 231–239.
- Koo, B.W., Hebda, J.A., Miranker, A.D., 2008. Amide inequivalence in the fibrillar assembly of islet amyloid polypeptide. *Protein Eng. Des. Sel.* 21, 147–154.
- Laghaei, R., Mousseau, N., Wei, G., 2011. Structure and thermodynamics of amylin dimer studied by Hamiltonian-temperature replica exchange molecular dynamics simulations. *J. Phys. Chem. B* 115, 3146–3154.
- Leslie, A.G.W., Powell, H.R., 2007. Processing diffraction data with mosflm. In: Read, R., Sussman, J.L. (Eds.), *Evolving Methods for Macromolecular Crystallography*. Springer, Dordrecht, The Netherlands, pp. 41–51.
- Liang, G., Zhao, J., Yu, X., Zheng, J., 2013a. Comparative molecular dynamics study of human islet amyloid polypeptide (IAPP) and rat IAPP oligomers. *Biochemistry* 52, 1089–1100.
- Liang, G., Zhao, J., Yu, X., Zheng, J., 2013b. Comparative Molecular Dynamics Study of Human Islet Amyloid Polypeptide (IAPP) and Rat IAPP Oligomers. *Biochemistry* 52, 1089–1100.
- Louros, N.N., Iconomidou, V.A., Tsiolaki, P.L., Chrysinia, E.D., Baltatzis, G.E., Patsouris, E.S., Hamodrakas, S.J., 2014. An N-terminal pro-atrial natriuretic peptide (NT-proANP) ‘aggregation-prone’ segment involved in isolated atrial amyloidosis. *FEBS Lett.* 588, 52–57.

- Louros, N.N., Tsiolaki, P.L., Griffin, M.D., Howlett, G.J., Hamodrakas, S.J., Iconomidou, V.A., 2015a. Chameleon 'aggregation-prone' segments of apoA-I: a model of amyloid fibrils formed in apoA-I amyloidosis. *Int. J. Biol. Macromol.* 79, 711–718.
- Louros, N.N., Tsiolaki, P.L., Zompra, A.A., Pappa, E.V., Magafa, V., Pairas, G., Cordopatis, P., Cheimonidou, C., Trougakos, I.P., Iconomidou, V.A., Hamodrakas, S.J., 2015b. Structural studies and cytotoxicity assays of "aggregation-prone" IAPP(8–16) and its non-amyloidogenic variants suggest its important role in fibrillogenesis and cytotoxicity of human amylin. *Biopolymers* 104, 196–205.
- Luca, S., Yau, W.M., Leapman, R., Tycko, R., 2007. Peptide conformation and supramolecular organization in amylin fibrils: constraints from solid-state NMR. *Biochemistry* 46, 13505–13522.
- Lutz, T.A., 2010. The role of amylin in the control of energy homeostasis. *Am. J. Physiol.* 298, R1475–1484.
- Madine, J., Jack, E., Stockley, P.G., Radford, S.E., Serpell, L.C., Middleton, D.A., 2008. Structural insights into the polymorphism of amyloid-like fibrils formed by region 20–29 of amylin revealed by solid-state NMR and X-ray fiber diffraction. *J. Am. Chem. Soc.* 130, 14990–15001.
- Mao, Y., Yu, L., Yang, R., Ma, C., Qu, L.-B., Harrington, P.D.B., 2016. New insights into side effect of solvents on the aggregation of human islet amyloid polypeptide 11–20. *Talanta* 148, 380–386.
- Marek, P., Abedini, A., Song, B., Kanungo, M., Johnson, M.E., Gupta, R., Zaman, W., Wong, S.S., Raleigh, D.P., 2007. Aromatic interactions are not required for amyloid fibril formation by islet amyloid polypeptide but do influence the rate of fibril formation and fibril morphology. *Biochemistry* 46, 3255–3261.
- Mazor, Y., Gilead, S., Benhar, I., Gazit, E., 2002. Identification and characterization of a novel molecular-recognition and self-assembly domain within the islet amyloid polypeptide. *J. Mol. Biol.* 322, 1013–1024.
- Mirkin, N.G., Krimm, S., 1991. Ab initio vibrational analysis of hydrogen-bonded trans- and cis-N-methylacetamide. *J. Am. Chem. Soc.* 113, 9742–9747.
- Miyamoto, S., Kollman, P.A., 1992. Settle: an analytical version of the SHAKE and RATTLE algorithm for rigid water models. *J. Comput. Chem.* 13, 952–962.
- Moriarty, D.F., Raleigh, D.P., 1999. Effects of sequential proline substitutions on amyloid formation by human amylin20–29. *Biochemistry* 38, 1811–1818.
- Nakanishi, M., Takesada, H., Tsuboi, M., 1974. Letter: conformation of the cystine linkages in bovine alpha-lactalbumin as revealed by its Raman effect. *J. Mol. Biol.* 89, 241–243.
- Nanga, R.P., Brender, J.R., Xu, J., Hartman, K., Subramanian, V., Ramamoorthy, A., 2009. Three-dimensional structure and orientation of rat islet amyloid polypeptide protein in a membrane environment by solution NMR spectroscopy. *J. Am. Chem. Soc.* 131, 8252–8261.
- Nanga, R.P., Brender, J.R., Vivekanandan, S., Ramamoorthy, A., 2011. Structure and membrane orientation of IAPP in its natively amidated form at physiological pH in a membrane environment. *Biochim. Biophys. Acta* 1808, 2337–2342.
- Nilsson, M.R., 2004. Techniques to study amyloid fibril formation in vitro. *Methods* 34, 151–160.
- Ortiz, C., Zhang, D., Ribbe, A.E., Xie, Y., Ben-Amotz, D., 2007. Analysis of insulin amyloid fibrils by Raman spectroscopy. *Biophys. Chem.* 128, 150–155.
- Oxford diffraction, 2009. Chrysalis promotions. Oxford Diffraction Ltd., Abingdon, Oxfordshire, England.
- Pandit, A., Fay, N., Bordes, L., Valery, C., Cherif-Cheikh, R., Robert, B., Artzner, F., Paternostre, M., 2008. Self-assembly of the octapeptide lanreotide and lanreotide-based derivatives: the role of the aromatic residues. *J. Peptide Sci.* 14, 66–75.
- Patel, H.R., Pithadia, A.S., Brender, J.R., Fierke, C.A., Ramamoorthy, A., 2014. In search of aggregation pathways of IAPP and other amyloidogenic proteins: finding answers through NMR spectroscopy. *J. Phys. Chem. Lett.* 5, 1864–1870.
- Phillips, J.C., Braun, R., Wang, W., Gumbart, J., Tajkhorshid, E., Villa, E., Chipot, C., Skeel, R.D., Kale, L., Schulten, K., 2005. Scalable molecular dynamics with NAMD. *J. Comput. Chem.* 26, 1781–1802.
- Ratner, R.E., Dickey, R., Fineman, M., Maggs, D.G., Shen, L., Strobel, S.A., Weyer, C., Kolterman, O.G., 2004. Amylin replacement with pramlintide as an adjunct to insulin therapy improves long-term glycaemic and weight control in Type 1 diabetes mellitus: a 1-year, randomized controlled trial. *Diabetic Med.* 21, 1204–1212.
- Rodriguez-Perez, J.C., Hamley, I.W., Squires, A.M., 2013. Determination of orientations of aromatic groups in self-assembled peptide fibrils by polarized Raman spectroscopy. *Phys. Chem. Chem. Phys.* 15, 13940–13950.
- Romhanyi, G., 1971. Selective differentiation between amyloid and connective tissue structures based on the collagen specific topo-optical staining reaction with congo red. *Virchows Arch.* 354, 209–222.
- Rousseau, M.E., Lefevre, T., Beaulieu, L., Asakura, T., Pezolet, M., 2004. Study of protein conformation and orientation in silkworm and spider silk fibers using Raman microspectroscopy. *Biomacromolecules* 5, 2247–2257.
- Ryckaert, J.-P., Ciccotti, G., Berendsen, H.J.C., 1977. Numerical integration of the cartesian equations of motion of a system with constraints: molecular dynamics of n-alkanes. *J. Comput. Phys.* 23, 327–341.
- Sakagashira, S., Hiddinga, H.J., Tateishi, K., Sanke, T., Hanabusa, T., Nanjo, K., Eberhardt, N.L., 2000. S20G mutant amylin exhibits increased in vitro amyloidogenicity and increased intracellular cytotoxicity compared to wild-type amylin. *Am. J. Pathol.* 157, 2101–2109.
- Sant'Anna, R., Braga, C., Varejao, N., Pimenta, K.M., Grana-Montes, R., Alves, A., Cortines, J., Cordeiro, Y., Ventura, S., Foguel, D., 2014. The importance of a gatekeeper residue on the aggregation of transthyretin: implications for transthyretin-related amyloidosis. *J. Biol. Chem.* 289, 28324–28337.
- Sciaccia, M.F., Lolicato, F., Di Mauro, G., Milardi, D., D'Urso, L., Satriano, C., Ramamoorthy, A., La Rosa, C., 2016. The role of cholesterol in driving IAPP-membrane interactions. *Biophys. J.* 111, 140–151.
- Scrocchi, L.A., Ha, K., Chen, Y., Wu, L., Wang, F., Fraser, P.E., 2003. Identification of minimal peptide sequences in the (8–20) domain of human islet amyloid polypeptide involved in fibrillogenesis. *J. Struct. Biol.* 141, 218–227.
- Sereda, V., Sawaya, M.R., Lednev, I.K., 2015. Structural organization of insulin fibrils based on polarized Raman spectroscopy: evaluation of existing models. *J. Am. Chem. Soc.* 137, 11312–11320.
- Shim, S.H., Gupta, R., Ling, Y.L., Strasfeld, D.B., Raleigh, D.P., Zanni, M.T., 2009. Two-dimensional IR spectroscopy and isotope labeling defines the pathway of amyloid formation with residue-specific resolution. *Proc. Natl. Acad. Sci. U.S.A.* 106, 6614–6619.
- Siamwiza, M.N., Lord, R.C., Chen, M.C., Takamatsu, T., Harada, I., Matsuura, H., Shimanouchi, T., 1975. Interpretation of the doublet at 850 and 830 cm<sup>-1</sup> in the Raman spectra of tyrosyl residues in proteins and certain model compounds. *Biochemistry* 14, 4870–4876.
- Sugeta, H., 1975. Normal vibrations and molecular conformations of dialkyl disulfides. *Spectrochim. Acta, Part A* 31, 1729–1737.
- Sugeta, H., Go, A., Miyazawa, T., 1972. S-S and C-S stretching vibrations and molecular conformations of dialkyl disulfides and cystine. *Chem. Lett.* 1, 83–86.
- Sugeta, H., Go, A., Miyazawa, T., 1973. Vibrational spectra and molecular conformations of dialkyl disulfides. *Bull. Chem. Soc. Jpn.* 46, 3407–3411.
- Tian, J., Wu, N., Guo, J., Fan, Y., 2009. Prediction of amyloid fibril-forming segments based on a support vector machine. *BMC Bioinf.* 10 (Suppl. 1), S45.
- Tsolis, A.C., Papandreou, N.C., Iconomidou, V.A., Hamodrakas, S.J., 2013. A consensus method for the prediction of 'aggregation-prone' peptides in globular proteins. *PLoS One* 8, e54175.
- Tu, L.H., Serrano, A.L., Zanni, M.T., Raleigh, D.P., 2014. Mutational analysis of preamyloid intermediates: the role of his-tyr interactions in islet amyloid formation. *Biophys. J.* 106, 1520–1527.
- Van Wart, H.E., Scheraga, H.A., 1976. Raman spectra of strained disulfides. Effect of rotation about sulfur-sulfur bonds on sulfur-sulfur stretching frequencies. *J. Phys. Chem.* 80, 1823–1832.
- Van Wart, H.E., Lewis, A., Scheraga, H.A., Saeva, F.D., 1973. Disulfide bond dihedral angles from Raman spectroscopy. *Proc. Natl. Acad. Sci.* 70, 2619–2623.
- vandenAkker, C.C., Deckert-Gaudig, T., Schleeper, M., Velikov, K.P., Deckert, V., Bonn, M., Koenderink, G.H., 2015. Nanoscale heterogeneity of the molecular structure of individual hIAPP amyloid fibrils revealed with tip-enhanced Raman spectroscopy. *Small* 11, 4131–4139.
- Wang, M., Yang, J., Wang, J., Wang, X., 2012. Structural effects of L16Q, S20G, and L16Q-S20G mutations on hIAPP: a comparative molecular dynamics study. *Chin. J. Chem.* 30, 241–248.
- Wang, H., Ridgway, Z., Cao, P., Ruzsicska, B., Raleigh, D.P., 2015. Analysis of the ability of pramlintide to inhibit amyloid formation by human islet amyloid polypeptide reveals a balance between optimal recognition and reduced amyloidogenicity. *Biochemistry* 54, 6704–6711.
- Westermark, P., Wilander, E., 1978. The influence of amyloid deposits on the islet volume in maturity onset diabetes mellitus. *Diabetologia* 15, 417–421.
- Westermark, P., Wernstedt, C., O'Brien, T.D., Hayden, D.W., Johnson, K.H., 1987a. Islet amyloid in type 2 human diabetes mellitus and adult diabetic cats contains a novel putative polypeptide hormone. *A. J. Pathol.* 127, 414–417.
- Westermark, P., Wernstedt, C., Wilander, E., Hayden, D.W., O'Brien, T.D., Johnson, K.H., 1987b. Amyloid fibrils in human insulinoma and islets of Langerhans of the diabetic cat are derived from a neuropeptide-like protein also present in normal islet cells. *Proc. Natl. Acad. Sci. U.S.A.* 84, 3881–3885.
- Westermark, P., Engstrom, U., Johnson, K.H., Westermark, G.T., Betsholtz, C., 1990. Islet amyloid polypeptide: pinpointing amino acid residues linked to amyloid fibril formation. *Proc. Natl. Acad. Sci. U.S.A.* 87, 5036–5040.
- Williamson, J.A., Miranker, A.D., 2007. Direct detection of transient alpha-helical states in islet amyloid polypeptide. *Protein Sci.* 16, 110–117.
- Wiltzius, J.J., Sievers, S.A., Sawaya, M.R., Cascio, D., Popov, D., Riek, C., Eisenberg, D., 2008. Atomic structure of the cross-beta spine of islet amyloid polypeptide (amylin). *Protein Sci.* 17, 1467–1474.
- Xu, W., Jiang, P., Mu, Y., 2009. Conformation preorganization: effects of S20G mutation on the structure of human islet amyloid polypeptide segment. *J. Phys. Chem. B* 113, 7308–7314.